A generalized Hellinger-Reissner variational principle and its PFEM formulation for dynamic analysis of saturated porous media

Liang Wang[1], Xue Zhang[2*], Sheng Zhang[3], Stefano Tinti[1]

[1]Dipartimento di Fisica e Astronomia (DIFA), Settore di Geofisica, Università di Bologna, Bologna, Italy

[2]Department of Civil Engineering and Industrial Design, University of Liverpool, Liverpool, UK

[3] School of Civil Engineering, Central South University, Changsha, China

[*]Corresponding author: Xue Zhang (Xue.Zhang2@liverpool.ac.uk).

Abstract.

In this paper, a novel mathematical programming formulation is derived based on the ***u***-*p* form for the dynamic analysis of saturated porous media. The mixed finite element is used for the interpolation of field variables and after discretization the formulation is remolded into a standard second-order cone programming problem that can be resolved using modern optimization engines. The proposed optimization-based computational scheme is verified against typical benchmarks such as the dynamic consolidation problem and the wave propagation in saturated soils. To tackle issues such as mesh distortions and severe free-surface evolutions resulting from large deformations, the scheme is further implemented into the PFEM framework. The capability of the proposed method for analyzing porous media with large deformations is illustrated by modelling the collapse of a saturated granular column in air and the post-failure of an embankment due to seepage with results being compared to the ones from lab tests and the modelling using other numerical approaches such as the material point method and the smoothed particle hydrodynamics method.

Keywords: Saturated porous media; dynamic finite element analysis; mathematical programming; particle finite element method

1 Introduction

Although the finite element method (FEM) has obtained a strong position in geotechnical analysis and design, the standard Lagrangian FEM has its limitations when it comes to geotechnical problems with large deformations and free-surface evolutions. Owing to the fixed mesh topology, the standard Lagrangian FEM cannot capture severe free-surface evolutions as occur in problems such as landslides, debris flows and pile installation. Excessive mesh distortions are also inevitable when geo-materials undergo large deformations which deteriorate the accuracy of the FEM analysis and even result in non-convergence issues.

Because of the limitations of the standard Lagrangian FEM, a series of advanced continuum numerical approaches have been developed in the past decades and applied to large deformation geotechnical problems. Representatives include, but are not limited to, the unconventional finite element techniques, such as the Arbitrary Lagrangian-Eulerian (ALE) method [1] and the Coupled Eulerian Lagrangian (CEL) method, and approaches of particle natures, such as the Smoothed Particle Hydrodynamics (SPH) method [2,3], the Material Point Method (MPM) [4,5], and the Particle Finite Element Method (PFEM) [6,7]. Among them, the PFEM is attracting increasing attention from the community of geotechnical engineering. As a mixture of the FEM and the particle approach, the PFEM was originally invented for solving free-surface flow problems [8,9]. It adopts particles, which are in fact mesh nodes, to represent materials. At each analysis step, the computational domain is identified first based on the particles followed by the mesh generation via triangulation of the identified domain. Afterward, solutions are pursued using the standard FEM over the mesh. By doing so, the PFEM inherits both the solid mathematical foundation of the standard FEM and the flexibility of particle approaches for handling extreme deformations. To date, a series of geotechnical problems that are challenging to the standard FEM have been simulated successfully using the PFEM, for example ground excavations [10], granular flows [11–13], subaerial/submarine landslides [14–17], debris flows [18], soil-structure interactions [18], penetration problems [19], etc.

Despite the contributions to the PFEM in geotechnical engineering, most versions developed are limited to the case of undrained conditions that total stress analysis is performed. Only very recently, the PFEM was extended for analyzing coupled hydro-mechanical processes based on effective stresses, for instance, the effective stress analysis of foundation penetration into saturated soils [20] and consolidation of saturated soils [21]. Saturated soils are assumed to behave under quasi-static conditions in these works implying dynamic effects are neglected. Although quasi-static conditions apply to many cases, there are geotechnical problems where dynamic effects are not negligible such as stress wave propagation in soils, debris flows, landslides, etc.

In this paper, a version of the PFEM is developed for saturated soil dynamics.

Specifically, a generalized Hellinger-Reissner (HR) variational principle is proposed for dynamic analysis of saturated porous media. After discretization using mixed finite elements, the principle is reformed as a standard second-order cone programming (SOCP) problem that can be solved using the interior-point method. Compared to the conventional FEM algorithm developed based on the Newton-Raphson iteration scheme, the FEM in SOCP has advantages including the possibility of analyses of convergence properties of solutions [22,23], straightforward treatment of singularities in the Mohr-Coulomb model [24] and the the Bingham model [17], and the forthright extension from single-surface plasticity to multi-surface plasticity. The generalized HR variational principle for solid and fluid dynamics and the corresponding FE formulation in SOCP have been constructed in [17]. The hydro-mechanical effects will be further considered in this framework in this paper with the resulting FE formulation in SOCP being merged into the PFEM for saturated soil dynamics with large deformations and free-surface evolutions.

2 Hellinger-Reissner variational principle for static elasticity

While algorithms for finite element analysis are commonly derived from the principle of virtual work where displacements are the sole master field, multi-field variational principles can also be adopted for this purpose [25].

For static elasticity of a solid, the Hellinger-Reissner functional is expressed as

$$\Pi(\boldsymbol{\sigma},\boldsymbol{u}) = \int_\Omega \left(-\frac{1}{2}\boldsymbol{\sigma}^T\mathbb{C}\boldsymbol{\sigma} + \boldsymbol{\sigma}^T\boldsymbol{S}\boldsymbol{u}\right)d\Omega - \int_\Omega \boldsymbol{b}^T\boldsymbol{u}d\Omega - \int_\Gamma \boldsymbol{t}^T\boldsymbol{u}d\Gamma \tag{1}$$

where $\boldsymbol{\sigma}$ is the Cauchy stress, $\boldsymbol{u}$ is the displacement, $\boldsymbol{b}$ is the body force, $\boldsymbol{t}$ is the traction, $\mathbb{C}$ is the elastic compliance matrix, and the operator $\boldsymbol{S}$ takes the form

$$\boldsymbol{S} = [\frac{\partial}{\partial x}\ 0\ 0\ \frac{\partial}{\partial y};0\ \frac{\partial}{\partial y}\ 0\ \frac{\partial}{\partial x}]^T \tag{2}$$

In functional (1), both the displacement $\boldsymbol{u}$ and the stresses $\boldsymbol{\sigma}$ are master fields. The variation of the functional $\delta\Pi(\boldsymbol{\sigma},\boldsymbol{u}) = 0$ leads to a pair of the stress and the displacement which is at a saddle point of the functional. This is in contrast to the FEM based on virtual work that the variation results in a point for the extreme value of the functional. The problem hence falls in the min-max optimization category:

$$\min_{\boldsymbol{u}}\ \max_{\boldsymbol{\sigma}}\ -\frac{1}{2}\int_\Omega \boldsymbol{\sigma}^T\mathbb{C}\boldsymbol{\sigma}d\Omega + \int_\Omega \boldsymbol{\sigma}^T\boldsymbol{S}\boldsymbol{u}d\Omega - \int_\Omega \boldsymbol{b}^T\boldsymbol{u}d\Omega - \int_\Gamma \boldsymbol{t}^T\boldsymbol{u}d\Gamma \tag{3}$$

Based on the HR variational principle for elasticity, the generalized HR variational principles have been developed for analysing elastoplastic problems, elastoviscoplastic problems, and quasi-static poro-elastoplastic problems [6,17,26,27]. In this work, the Hellinger-Reissner (HR) variational principle [28] is used to establish the finite element formulation for analyzing saturated porous media in dynamics.

3 Hellinger-Reissner variational principle for dynamic saturated porous media

The HR variational principle for dynamic elastoplastic analysis of saturated porous media is developed in this section.

3.1 Governing equations

The so-called $\boldsymbol{u}$-p model for dynamic analysis of saturated porous media is adopted. This model neglects the derivative of the relative velocity of fluid with respect to solid and is widely used for the case of low-frequency loading [29,30]. In a two-dimensional case, the governing equations for a saturated porous medium with a domain Ω and boundary Γ are as follows (see also Figure 1):

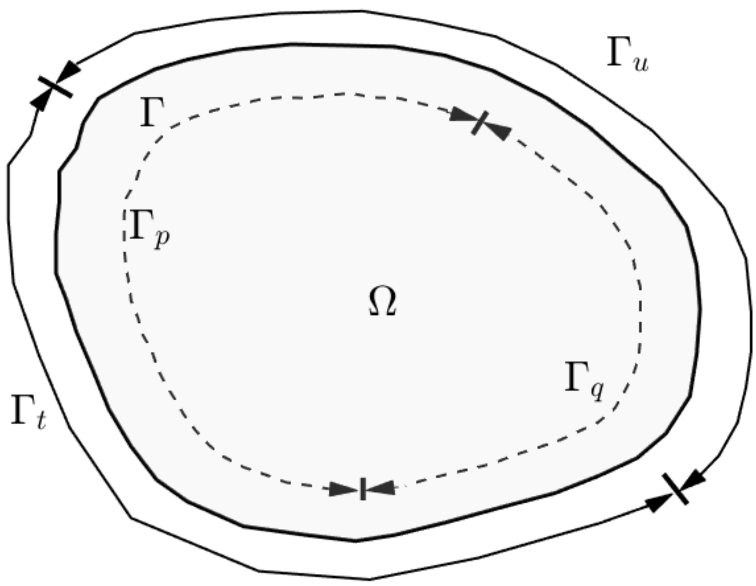

Figure 1. The domain of a saturated medium and its boundary partition. The surfaces Γ_u ,Γ_t , Γ_p and Γ_q are subjected to the prescribed displacement, traction, pore water pressure and fluid flux, respectively.

(a) Linear momentum balance equation for the mixture

$$\rho\ddot{\boldsymbol{u}} = \boldsymbol{S}^T(\boldsymbol{\sigma}' + \boldsymbol{m}p) + \boldsymbol{b} \tag{4}$$

(b) Darcy's law

$$\nabla p + \boldsymbol{b}_f - \frac{\gamma_f}{k}\boldsymbol{w} = \rho_f \ddot{\boldsymbol{u}} \tag{5}$$

(c) Mass balance equation of pore fluid

$$\nabla^T \boldsymbol{w} + \nabla^T \dot{\boldsymbol{u}} = 0 \tag{6}$$

(d) Strain decomposition and stress-strain relationship

$$\boldsymbol{\varepsilon} = \boldsymbol{\varepsilon}^e + \boldsymbol{\varepsilon}^p \text{ where } \begin{cases} \boldsymbol{\varepsilon}^e = \mathbb{C}\boldsymbol{\sigma}' = \mathbb{C}(\boldsymbol{\sigma} - \boldsymbol{m}p), \\ \boldsymbol{\varepsilon}^p = 0 \ \text{ if } F < 0\,; \boldsymbol{\varepsilon}^p = \lambda \nabla_{\sigma'} G \ \text{ if } F = 0 \end{cases} \tag{7}$$

where

ρ is the density of mixture;

$\boldsymbol{u}$ is the displacement of the solid skeleton;

ρ_f is the density of fluid;

$\boldsymbol{\sigma}'$ is the effective stress acting on solid skeleton;

p is the pore water pressure with tensile pore water pressure being positive;

$\boldsymbol{b}$ is the body force of the mixture;

$\boldsymbol{b}_f$ is the body force of the fluid;

γ_f is the unit weight of the fluid;

k is the Darcy hydraulic conductivity;

$\boldsymbol{w}$ is the velocity of pore fluid relative to the solid skeleton;

$\boldsymbol{\varepsilon}$ is the strain vector defined as $\boldsymbol{\varepsilon} = \boldsymbol{S}\mathbf{u}$, consisting of $\boldsymbol{\varepsilon}^e$ (elastic strain) and $\boldsymbol{\varepsilon}^p$ (plastic strain);

λ is the plastic multiplier, $\lambda \geq 0$;

F is the yield function, $F \leq 0$;

G is the plastic potential;

$\mathbb{C}$ is the elastic compliance matrix;

$\boldsymbol{\sigma}$ is the total Cauchy stress of the mixture;

$\boldsymbol{m} = [1; 1; 1; 0]$.

The density of the mixture is $\rho = n_f\rho_f + (1 - n_f)\rho_s$ in which ρ_s and n_f are the density of solid and the porosity of the mixture, respectively. The superficial velocity

$\boldsymbol{w}$ in Eq. (6) can be eliminated by substituting Eq. (5):

$$\nabla^T \frac{k}{\gamma_f}(\nabla p + \boldsymbol{b}_f - \rho_f \ddot{\boldsymbol{u}}) + \nabla^T \dot{\boldsymbol{u}} = 0 \tag{8}$$

In addition to the governing equations (4), (7) and (8), the following boundary conditions (see also Figure 1) should be satisfied to complete the boundary-value problem

$$\boldsymbol{u} = \bar{\boldsymbol{u}} \text{ on } \Gamma_u \tag{9}$$

$$\boldsymbol{N}^T \boldsymbol{\sigma} = \bar{\boldsymbol{t}} \text{ on } \Gamma_t \tag{10}$$

$$p = \bar{p} \text{ on } \Gamma_p \tag{11}$$

$$\boldsymbol{N}^T \frac{k}{\gamma_f}(\nabla p + \boldsymbol{b}_f - \rho_f \ddot{\boldsymbol{u}}) = \bar{q} \text{ on } \Gamma_q \tag{12}$$

where $\bar{\boldsymbol{u}}$, $\bar{\boldsymbol{t}}$, $\bar{p}$ and $\bar{q}$ are the prescribed displacements, tractions, pore water pressure and fluid flux. $\boldsymbol{N}$ is the outward vector normal to the corresponding surface of the boundary.

3.2 Time discretization

The standard θ-method is introduced for the time discretization of the effective stress $\boldsymbol{\sigma'}$, the velocity $\boldsymbol{v}$ and the pressure p:

$$\boldsymbol{\sigma'} = \theta_1 \boldsymbol{\sigma}'_{n+1} + (1-\theta_1)\boldsymbol{\sigma}'_n \tag{13}$$

$$\boldsymbol{v} = \frac{\Delta \boldsymbol{u}}{\Delta t} = \theta_2 \boldsymbol{v}_{n+1} + (1-\theta_2)\boldsymbol{v}_n \tag{14}$$

$$p = \theta_3 p_{n+1} + (1-\theta_3) p_n \tag{15}$$

The subscripts n and n+1 denote the known and unknown states, respectively, and Δt is the time increment. The governing equations (4) and (8) can then be re-arranged as:

$$\boldsymbol{S}^T\boldsymbol{\sigma}'_{n+1} + \frac{(1-\theta_1)}{\theta_1}\boldsymbol{S}^T\boldsymbol{\sigma}'_n + \frac{\theta_3}{\theta_1}\boldsymbol{S}^T\boldsymbol{m}p_{n+1} + \frac{(1-\theta_3)}{\theta_1}\boldsymbol{S}^T\boldsymbol{m}p_n + \widetilde{\boldsymbol{b}} = \boldsymbol{\gamma}_{n+1} \tag{16}$$

$$\nabla^T\frac{k\theta_1}{\gamma_f}\left(\frac{\theta_3}{\theta_1}\nabla p_{n+1} + \widetilde{\boldsymbol{b}}_f\right) + \nabla^T\frac{\Delta\boldsymbol{u}}{\Delta t} = 0 \tag{17}$$

in which

$$\tilde{\rho} = \frac{\rho}{\theta_1\theta_2}, \widetilde{\boldsymbol{b}} = \frac{1}{\theta_1}\boldsymbol{b} + \tilde{\rho}\frac{\boldsymbol{v}_n}{\Delta t},\ \boldsymbol{\gamma}_{n+1} = \tilde{\rho}\frac{\Delta\boldsymbol{u}}{\Delta t^2} \tag{18}$$

$$\tilde{\rho}_f = \frac{\rho_f}{\theta_1},\ \widetilde{\boldsymbol{b}}_f = \frac{1}{\theta_1}\boldsymbol{b}_f + \frac{(1-\theta_3)}{\theta_1}\nabla p_n - \tilde{\rho}_f\ddot{\boldsymbol{u}} \tag{19}$$

Note that the term $\tilde{\rho}_f\ddot{\boldsymbol{u}}$ in Eq. (19) is calculated based on the known velocity field that $\tilde{\rho}_f\ddot{\boldsymbol{u}} = \tilde{\rho}_f\frac{\boldsymbol{v}_n-\boldsymbol{v}_{n-1}}{\Delta t}$ for the sake of simplicity. The traction boundary condition (10) and the fluid flux boundary condition (12) are rendered as:

$$\boldsymbol{N}^T\left(\boldsymbol{\sigma}'_{n+1} + \frac{\theta_3}{\theta_1}\boldsymbol{m}p_{n+1}\right) + \frac{(1-\theta_1)}{\theta_1}\boldsymbol{N}^T\boldsymbol{\sigma}'_n + \frac{(1-\theta_3)}{\theta_1}\boldsymbol{N}^T\boldsymbol{m}p_n = \tilde{\boldsymbol{t}},\ \tilde{\boldsymbol{t}} = \frac{1}{\theta_1}\bar{\boldsymbol{t}} \tag{20}$$

$$\boldsymbol{N}^T\frac{k\theta_1}{\gamma_f}\left(\frac{\theta_3}{\theta_1}\nabla p_{n+1} + \widetilde{\boldsymbol{b}}_f\right) = \bar{q} \tag{21}$$

3.3 Min-max problem

Following [6,27], the min-max problem equivalent to the time-discretized governing equations for incremental dynamic analysis of saturated porous media can now be given:

$$
\begin{aligned}
\min_{\Delta\boldsymbol{u}}\ \max_{(\sigma',p,\gamma)_{n+1}}\ \Pi = & -\frac{1}{2}\int_\Omega \Delta\boldsymbol{\sigma}'^T\mathbb{C}\Delta\boldsymbol{\sigma}'d\Omega \\
& +\int_\Omega(\boldsymbol{\sigma}'_{n+1}+\frac{\theta_3}{\theta_1}\boldsymbol{m}p_{n+1})^T\boldsymbol{S}(\Delta\boldsymbol{u})d\Omega \\
& +\int_\Omega(\frac{1-\theta_1}{\theta_1}\boldsymbol{\sigma}'_n+\frac{1-\theta_3}{\theta_1}\boldsymbol{m}p_n)^T\boldsymbol{S}(\Delta\boldsymbol{u})d\Omega \\
& -\frac{\Delta t}{2}\int_\Omega(\frac{\theta_3}{\theta_1}\nabla p_{n+1}+\tilde{\boldsymbol{b}}_f)^T\frac{k\theta_1}{\gamma_f}(\frac{\theta_3}{\theta_1}\nabla p_{n+1}+\tilde{\boldsymbol{b}}_f)d\Omega \\
& -\int_\Omega\tilde{\boldsymbol{b}}^T\Delta\boldsymbol{u}d\Omega-\int_{\Gamma_t}\tilde{\boldsymbol{t}}^T\Delta\boldsymbol{u}d\Gamma+\int_\Omega\boldsymbol{\gamma}_{n+1}^T\Delta\boldsymbol{u}d\Omega \\
& -\frac{\Delta t^2}{2}\int_\Omega\boldsymbol{\gamma}_{n+1}^T\tilde{\rho}^{-1}\boldsymbol{\gamma}_{n+1}d\Omega-\Delta t\int_{\Gamma_q}\frac{\theta_3}{\theta_1}p_{n+1}\bar{q}d\Gamma
\end{aligned}
$$

$$
\text{subject to}\quad F(\boldsymbol{\sigma}'_{n+1})\le 0 \tag{22}
$$

The validity of this min-max problem can be demonstrated by showing the associated Karush-Kuhn-Tucher (KKT) conditions. To this end, the Lagrangian of the problem (22) is first constructed, which is

$$
\begin{aligned}
\mathcal{L} = & -\frac{1}{2}\int_\Omega\Delta\boldsymbol{\sigma}'^T\mathbb{C}\Delta\boldsymbol{\sigma}'d\Omega+\int_\Omega(\boldsymbol{\sigma}'_{n+1}+\frac{\theta_3}{\theta_1}\boldsymbol{m}p_{n+1})^T\boldsymbol{S}(\Delta\boldsymbol{u})d\Omega \\
& +\int_\Omega(\frac{1-\theta_1}{\theta_1}\boldsymbol{\sigma}'_n+\frac{1-\theta_3}{\theta_1}\boldsymbol{m}p_n)^T\boldsymbol{S}(\Delta\boldsymbol{u})d\Omega \\
& -\frac{\Delta t}{2}\int_\Omega(\frac{\theta_3}{\theta_1}\nabla p_{n+1}+\tilde{\boldsymbol{b}}_f)^T\frac{k\theta_1}{\gamma_f}(\frac{\theta_3}{\theta_1}\nabla p_{n+1}+\tilde{\boldsymbol{b}}_f)d\Omega \\
& -\int_\Omega\tilde{\boldsymbol{b}}^T\Delta\boldsymbol{u}d\Omega-\int_{\Gamma_t}\tilde{\boldsymbol{t}}^T\Delta\boldsymbol{u}d\Gamma+\int_\Omega\boldsymbol{\gamma}_{n+1}^T\Delta\boldsymbol{u}d\Omega-\frac{\Delta t^2}{2}\int_\Omega\boldsymbol{\gamma}_{n+1}^T\tilde{\rho}^{-1}\boldsymbol{\gamma}_{n+1}d\Omega \\
& -\Delta t\int_{\Gamma_q}\frac{\theta_3}{\theta_1}p_{n+1}\bar{q}d\Gamma+\int_\Omega\Delta\lambda F(\boldsymbol{\sigma}'_{n+1})d\Omega
\end{aligned} \tag{23}
$$

Following [31], the KKT conditions of (22) can be derived which are

- Stationarity

$$\frac{\partial \mathcal{L}}{\partial \Delta \boldsymbol{u}} = \begin{cases} \boldsymbol{S}^T(\boldsymbol{\sigma}'_{n+1} + \frac{\theta_3}{\theta_1}\boldsymbol{m}p_{n+1}) + \quad \boldsymbol{S}^T(\frac{1-\theta_1}{\theta_1}\boldsymbol{\sigma}'_n + \frac{1-\theta_3}{\theta_1}\boldsymbol{m}p_n) + \widetilde{\boldsymbol{b}} = \boldsymbol{\gamma}_{n+1} & \text{in } \Omega \\ \boldsymbol{N}^T(\boldsymbol{\sigma}'_{n+1} + \frac{\theta_3}{\theta_1}\boldsymbol{m}p_{n+1}) + \quad \boldsymbol{N}^T(\frac{1-\theta_1}{\theta_1}\boldsymbol{\sigma}'_n + \frac{1-\theta_3}{\theta_1}\boldsymbol{m}p_n) \ = \tilde{\boldsymbol{t}} & \text{on } \Gamma_t \end{cases} \tag{24}$$

$$\frac{\partial \mathcal{L}}{\partial \boldsymbol{\sigma}'_{n+1}} = \boldsymbol{S}(\Delta \boldsymbol{u}) - \mathbb{C}\Delta\boldsymbol{\sigma}'_{n+1} - \Delta\lambda \frac{\partial F}{\partial \boldsymbol{\sigma}'_{n+1}} = \boldsymbol{0} \tag{25}$$

$$\frac{\partial \mathcal{L}}{\partial p_{n+1}} = \begin{cases} \nabla^T(\Delta \boldsymbol{u}) + \Delta t \nabla^T \frac{k\theta_1}{\gamma_f}(\frac{\theta_3}{\theta_1}\nabla p_{n+1} + \widetilde{\boldsymbol{b}}_f) = \boldsymbol{0} & \text{in } \Omega \\ \boldsymbol{N}^T \frac{k\theta_1}{\gamma_f}(\frac{\theta_3}{\theta_1}\nabla p_{n+1} + \widetilde{\boldsymbol{b}}_f) \ = \bar{q} & \text{on } \Gamma_q \end{cases} \tag{26}$$

$$\frac{\partial \mathcal{L}}{\partial \boldsymbol{\gamma}_{n+1}} = \Delta \boldsymbol{u} - \Delta t^2 \tilde{\rho}^{-1} \boldsymbol{\gamma}_{n+1} = 0 \tag{27}$$

- Complementary slackness

$$\Delta\lambda F(\boldsymbol{\sigma}'_{n+1}) = 0 \tag{28}$$

- Primal feasibility

$$F(\boldsymbol{\sigma}'_{n+1}) \leq 0 \tag{29}$$

- Dual feasibility

$$\Delta\lambda \geq 0 \tag{30}$$

Remark:

It is clear that

(24) consists of the discretized linear moment equilibrium equations of the mixture, Eq. (16), and the boundary condition in (20);

(25), (28)-(30) are the incremental form of the constitutive equations;

(26) indicates the governing equation in (17) and the boundary condition related to the fluid flux;

(27) is the expression for the dynamic force $\boldsymbol{\gamma}_{n+1}$.

Note that the above is for the associated plastic flow. The scheme proposed in [32] can be used in order to consider non-associated flow rules. Specifically, for two-dimensional cases, the yield function F and the plastic potential G for non-associated Mohr-Coulomb model are given as

$$F = \sqrt{\left(\sigma'_{xx} - \sigma'_{yy}\right)^2 + 4\sigma'^2_{xy}} + \left(\sigma'_{xx} + \sigma'_{yy}\right)\sin\varphi' - 2c'\cos\varphi' \tag{31}$$

$$G = \sqrt{\left(\sigma'_{xx} - \sigma'_{yy}\right)^2 + 4\sigma'^2_{xy}} + \left(\sigma'_{xx} + \sigma'_{yy}\right)\sin\psi \tag{32}$$

where φ' is the effective friction angle, c' is the effective cohesion, and ψ is the dilation angle. The associated computational schemes [32] implies that an approximate form of F is used ($F \approx F^* \rightarrow \frac{\partial F^*}{\partial \boldsymbol{\sigma}'_{n+1}} = \frac{\partial G}{\partial \boldsymbol{\sigma}'_{n+1}}$):

$$\begin{aligned} F \approx F^* = & \sqrt{\left(\sigma'_{xx} - \sigma'_{yy}\right)^2 + 4\sigma'^2_{xy}} + \left(\sigma'_{xx} + \sigma'_{yy}\right)\sin\psi \\ & + \left(\sigma'_{xx} + \sigma'_{yy}\right)_0 (\sin\varphi' - \sin\psi) - 2c'\cos\varphi' \\ = & \sqrt{\left(\sigma'_{xx} - \sigma'_{yy}\right)^2 + 4\sigma'^2_{xy}} + \left(\sigma'_{xx} + \sigma'_{yy}\right)\sin\psi - 2\tilde{c}'\cos\psi \end{aligned} \tag{33}$$

where $\tilde{c}'$ is treated as a constant and updated by

$$\tilde{c}' = c' \frac{\cos\varphi'}{cos\psi} + \frac{1}{2}\left(tan\psi - \frac{\sin\varphi'}{cos\psi}\right)\left(\sigma'_{xx} + \sigma'_{yy}\right)_0 \tag{34}$$

The subscript 0 in (34) represents the state solved from the last analysis step. Such an approximation has been validated against typical benchmarks in geotechnical problems [32–34].

4 Finite element discretization

The standard finite element discretization of the optimization problem (22) is carried out using a mixed triangular element in this section. The discretized optimization problem is then reformed as a standard second-order cone programming problem that can be resolved using available optimization engines.

4.1 The mixed triangular element

The mixed triangular element shown in Figure 2 is adopted for the discretization. In detail, the field variables are approximated as:

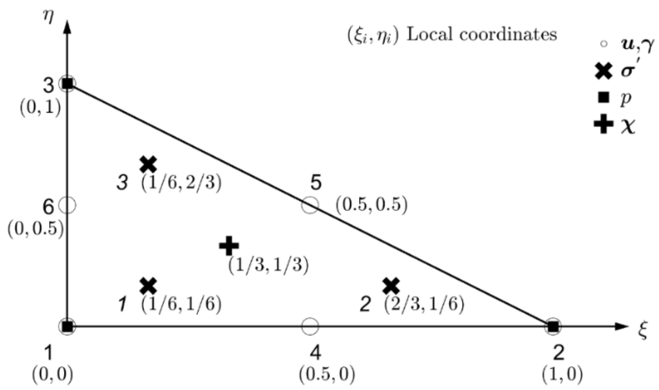

Figure 2. An illustration of the mixed triangular element.

$$\boldsymbol{\sigma} \approx \boldsymbol{N}_\sigma \hat{\boldsymbol{\sigma}} \tag{35}$$

$$\boldsymbol{u} \approx \boldsymbol{N}_u \hat{\boldsymbol{u}} \tag{36}$$

$$\boldsymbol{\gamma} \approx \boldsymbol{N}_\gamma \hat{\boldsymbol{\gamma}} \tag{37}$$

$$p \approx \boldsymbol{N}_p \hat{\boldsymbol{p}} \tag{38}$$

$$\boldsymbol{\chi} \approx \boldsymbol{N}_{\chi}\hat{\boldsymbol{\chi}} \tag{39}$$

where $\hat{\boldsymbol{\sigma}}$, $\hat{\boldsymbol{u}}$, $\hat{\boldsymbol{\Upsilon}}$ and $\hat{\boldsymbol{p}}$ are vectors consisting of the stress, displacement, dynamic force and pressure at element nodes. An intermediate variable $\boldsymbol{\chi}_{n+1} = \frac{\theta_3}{\theta_1}\nabla p_{n+1} + \tilde{\boldsymbol{b}}_f$ is introduced for brevity and $\hat{\boldsymbol{\chi}}$ is a vector of the intermediate variable at element nodes. $\boldsymbol{N}_{\sigma}$, $\boldsymbol{N}_{u}$, $\boldsymbol{N}_{\gamma}$, $\boldsymbol{N}_{p}$ and $\boldsymbol{N}_{\chi}$ are the matrices of the corresponding shape functions.

4.2 Discretized optimization problem

Substituting Eqs. (35)-(39) into the optimization problem (22) leads to its discretized form:

$$\begin{aligned}
\min_{\Delta\hat{\boldsymbol{u}}} \max_{(\hat{\boldsymbol{\sigma}},\hat{\boldsymbol{p}},\hat{\boldsymbol{\chi}},\hat{\boldsymbol{\gamma}},\hat{\boldsymbol{r}})_{n+1}} \quad & -\frac{1}{2}\Delta\hat{\boldsymbol{\sigma}}'^{T}\boldsymbol{C}\Delta\hat{\boldsymbol{\sigma}}' - \frac{1}{2}\Delta t^{2}\hat{\boldsymbol{\gamma}}_{n+1}^{T}\boldsymbol{D}\hat{\boldsymbol{\gamma}}_{n+1} \\
& -\frac{\Delta t}{2}\hat{\boldsymbol{\chi}}_{n+1}^{T}\boldsymbol{K}\hat{\boldsymbol{\chi}}_{n+1} + \Delta\hat{\boldsymbol{u}}^{T}\boldsymbol{B}^{T}\hat{\boldsymbol{\sigma}}_{n+1} \\
& +\Delta\hat{\boldsymbol{u}}^{T}\boldsymbol{A}_{p}^{T}\hat{\boldsymbol{p}}_{n+1} + \Delta\hat{\boldsymbol{u}}^{T}\boldsymbol{A}^{T}\hat{\boldsymbol{\gamma}}_{n+1} - \Delta\hat{\boldsymbol{u}}^{T}\tilde{\boldsymbol{f}}^{e} \\
& -\Delta t\hat{p}_{n+1}^{T}\boldsymbol{f}^{q} + \underline{(\boldsymbol{E}_{u}\hat{\boldsymbol{u}}^{p})^{T}\hat{\boldsymbol{r}}_{n+1}} - \underline{\Delta\hat{\boldsymbol{u}}^{T}\boldsymbol{E}_{u}\hat{\boldsymbol{r}}_{n+1}} \\
\text{subject to} \quad & F^{*}\left(\hat{\boldsymbol{\sigma}}_{n+1}^{j}\right) \leq 0, \quad j = 1, \dots, n_{\sigma} \\
& \boldsymbol{I}_{\chi}\hat{\boldsymbol{\chi}}_{n+1} - \boldsymbol{B}_{p}\hat{\boldsymbol{p}}_{n+1} = \tilde{\boldsymbol{f}}^{b}
\end{aligned} \tag{40}$$

where n_{σ} is the total number of Gauss integration points and

$$\boldsymbol{C} = \int_{\Omega} \boldsymbol{N}_{\sigma}^{T} \mathbb{C} \boldsymbol{N}_{\sigma} d\Omega,$$

$$\boldsymbol{B} = \int_{\Omega} \boldsymbol{N}_{\sigma}^{T} \boldsymbol{B}_{u} d\Omega \text{ with } \boldsymbol{B}_{u} = \boldsymbol{S}\boldsymbol{N}_{u},$$

$$\boldsymbol{D} = \int_{\Omega} \boldsymbol{N}_{\gamma}^{T} \tilde{\rho}^{-1} \boldsymbol{N}_{\gamma} d\Omega,$$

$$\boldsymbol{K} = \int_{\Omega} \boldsymbol{N}_{\chi}^{T} \frac{k\theta_1}{\gamma_f} \boldsymbol{N}_{\chi} d\Omega,$$

$$\boldsymbol{A} = \int_{\Omega} \boldsymbol{N}_{\gamma}^{T} \boldsymbol{N}_{u} d\Omega,$$

$$\boldsymbol{A}_{p}^{T} = \frac{\theta_3}{\theta_1} \int_{\Omega} \boldsymbol{B}_{u}^{T} \boldsymbol{m} \boldsymbol{N}_{p} d\Omega,$$

$$\boldsymbol{I}_{\chi} = \int_{\Omega} \boldsymbol{N}_{\chi} \, d\Omega,$$

$$\tilde{\boldsymbol{f}}^{e} = \int_{\Omega} \boldsymbol{N}_{u}^{T} \tilde{\boldsymbol{b}} d\Omega + \int_{\Gamma_t} \boldsymbol{N}_{u}^{T} \tilde{\boldsymbol{t}} d\Gamma - \frac{(1-\theta_1)}{\theta_1} \boldsymbol{B}^{T} \hat{\boldsymbol{\sigma}}_{n} - \frac{1-\theta_3}{\theta_3} \boldsymbol{A}_{p}^{T} \hat{p}_{n} \,,$$

$$\boldsymbol{B}_{p} = \int_{\Omega} \frac{\theta_3}{\theta_1} \nabla \boldsymbol{N}_{p} \, d\Omega,$$

$$\tilde{\boldsymbol{f}}^{b} = \int_{\Omega} \tilde{\boldsymbol{b}}_{f} \, d\Omega,$$

$$\boldsymbol{f}^{q} = \frac{\theta_3}{\theta_1} \int_{\Gamma_q} \boldsymbol{N}_{p}^{T} \bar{q} d\Gamma$$

(41)

In (40), the underlined terms account for the displacement boundary condition, and the newly introduced variable $\boldsymbol{r}_{n+1}$ is the reaction force at the element nodes with prescribed displacements. $\boldsymbol{E}_u$ is the index matrix consisting of 1 and 0 indicating the nodes with/without prescribed displacements. To verify its correctness, the stationarity of the associated Lagrangian with respect to the field variable $\hat{\boldsymbol{r}}_{n+1}$ is derived

$$\frac{\partial \mathcal{L}}{\partial \hat{\boldsymbol{r}}_{n+1}} = \boldsymbol{E}_u \Delta \hat{\boldsymbol{u}} - \boldsymbol{E}_u \hat{\boldsymbol{u}}^p = 0 \tag{42}$$

where $\hat{\boldsymbol{u}}^p$ is the discretized form of the prescribed displacement $\bar{\boldsymbol{u}}$ and this relationship is obviously the displacement boundary condition in Eq. (9). For the min-max problem (40), the minimization part can be solved analytically leading to a maximization problem which is

$$\begin{aligned}
\max_{(\hat{\boldsymbol{\sigma}},\hat{\boldsymbol{p}},\hat{\boldsymbol{\chi}},\hat{\boldsymbol{\gamma}},\hat{\boldsymbol{r}})_{n+1}} \quad & -\frac{1}{2}\Delta\hat{\boldsymbol{\sigma}}'^T \boldsymbol{C} \Delta\hat{\boldsymbol{\sigma}}' - \frac{1}{2}\Delta t^2 \hat{\boldsymbol{\gamma}}_{n+1}^T \boldsymbol{D} \hat{\boldsymbol{\gamma}}_{n+1} - \frac{\Delta t}{2} \hat{\boldsymbol{\chi}}_{n+1}^T \boldsymbol{K} \hat{\boldsymbol{\chi}}_{n+1} \\
& + (\boldsymbol{E}_u \hat{\boldsymbol{u}}^p)^T \hat{\boldsymbol{r}}_{n+1} - \Delta t \hat{p}_{n+1}^T \boldsymbol{f}^q \\
\text{subject to} \quad & F^*\left(\hat{\boldsymbol{\sigma}}_{n+1}^j\right) \le 0, \quad j = 1, \dots, n_\sigma \\
& \boldsymbol{B}^T \hat{\boldsymbol{\sigma}}_{n+1} + \boldsymbol{A}^T \hat{\boldsymbol{\gamma}}_{n+1} + \boldsymbol{A}_p^T \hat{\boldsymbol{p}}_{n+1} - \boldsymbol{E}_u \hat{\boldsymbol{r}}_{n+1} = \tilde{\boldsymbol{f}}^e \\
& \boldsymbol{I}_\chi \hat{\boldsymbol{\chi}}_{n+1} - \boldsymbol{B}_p \hat{\boldsymbol{p}}_{n+1} = \tilde{\boldsymbol{f}}^b
\end{aligned} \tag{43}$$

4.3 Reformulated mathematical program

The discretized optimization problem (43) is reformulated as a standard second-order cone programming (SOCP) problem in this section. A standard SOCP problem is in the form

$$\min_{\boldsymbol{x}} \quad \boldsymbol{c}^T\boldsymbol{x}$$
$$\text{subject to} \quad \boldsymbol{ax} = \boldsymbol{b}$$
$$\boldsymbol{x} \in \mathcal{K} \tag{44}$$

where $\boldsymbol{x} = (x_1, x_2, \ldots, x_n)^T$ consists of field variables, $\boldsymbol{a}$, $\boldsymbol{b}$ and $\boldsymbol{c}$ are the matrices and vectors of factors, and $\mathcal{K}$ is a tensor product of second-order cones such that $\mathcal{K} = \mathcal{K}_1 \times \cdots \times \mathcal{K}_l$. The second-order cones can be in the type of:

- *Quadratic cone*:

$$\mathcal{K}_q^n = \left\{\boldsymbol{x} \in \mathbb{R}^n: x_1 \geq \sqrt{x_2^2 + \cdots + x_n^2}\right\} \tag{45}$$

or

- *Rotated quadratic cone*:

$$\mathcal{K}_r^n = \left\{\boldsymbol{x} \in \mathbb{R}^n: 2x_1x_2 \geq \sum_{j=3}^n x_j^2, x_1, x_2 \geq 0\right\} \tag{46}$$

As shown, the standard SOCP (44) is a minimization of a linear objective function subjected to linear constraints and/or second-order cones. Following the procedure in [34], the discretized maximization problem (43) can be reformulated as the following SOCP problem

$$\min_{(\hat{\boldsymbol{\sigma}},\hat{p},\hat{\chi},\hat{\boldsymbol{\gamma}},\hat{\boldsymbol{r}},s_1,s_2,s_3)_{n+1}} \quad s_1 + s_2 + s_3$$

$$-(\boldsymbol{E}_u\hat{\boldsymbol{u}}^p)^T\hat{\boldsymbol{r}}_{n+1} + \Delta t\hat{p}_{n+1}^T\boldsymbol{f}^q$$

subject to $$\boldsymbol{B}^T\hat{\boldsymbol{\sigma}}_{n+1} + \boldsymbol{A}^T\hat{\boldsymbol{\gamma}}_{n+1} + \boldsymbol{A}_p^T\hat{p}_{n+1} - \boldsymbol{E}_u\hat{\boldsymbol{r}}_{n+1} = \tilde{\boldsymbol{f}}^e$$

$$\boldsymbol{I}_\chi\hat{\boldsymbol{\chi}}_{n+1} - \boldsymbol{B}_p\hat{p}_{n+1} = \tilde{\boldsymbol{f}}^b$$

$$\Delta\hat{\boldsymbol{\sigma}}'^T\boldsymbol{C}\Delta\hat{\boldsymbol{\sigma}}' = \sum_{j=1}^{n_\sigma}(\boldsymbol{C}_j^{1/2}\Delta\hat{\boldsymbol{\sigma}}_j')^2 \ \leq 2s_1$$

$$\hat{\boldsymbol{\gamma}}_{n+1}^T\boldsymbol{D}\hat{\boldsymbol{\gamma}}_{n+1} = \sum_{j=1}^{n_\gamma}(\boldsymbol{D}_j^{1/2}\hat{\boldsymbol{\gamma}}_{n+1}^j)^2 \leq 2\frac{s_2}{\Delta t^2}$$

$$\hat{\boldsymbol{\chi}}_{n+1}^T\boldsymbol{K}\hat{\boldsymbol{\chi}}_{n+1} = \sum_{j=1}^{n_\chi}(\boldsymbol{K}_j^{1/2}\hat{\boldsymbol{\chi}}_{n+1}^j)^2 \leq 2\frac{s_3}{\Delta t}$$

$$(F^*(\hat{\boldsymbol{\sigma}}_{n+1}^j) \leq 0)\begin{cases} \boldsymbol{\rho}^j = \boldsymbol{H}\hat{\boldsymbol{\sigma}}_{n+1}^j + \boldsymbol{d} \\ \rho_1^j \geq \sqrt{(\rho_2^j)^2 + (\rho_3^j)^2} \end{cases}, \quad j = 1, \ldots, n_\sigma \tag{47}$$

In the above, $\boldsymbol{\rho}$, $\boldsymbol{H}$, $\boldsymbol{d}$ are determined according to the Mohr-Coulomb yield criteria (33):

$$\boldsymbol{\rho} = (\rho_1, \rho_2, \rho_3), \ \boldsymbol{\sigma} = (\sigma_{xx}', \sigma_{yy}', \sigma_{zz}', \sigma_{xy}') \tag{48}$$

$$\boldsymbol{H} = \begin{bmatrix} -sin\psi & -sin\psi & 0 & 0 \\ 1 & -1 & 0 & 0 \\ 0 & 0 & 0 & 2 \end{bmatrix} \text{ and } \boldsymbol{d} = [2\tilde{c}'\cos\psi, 0, 0]^T \tag{49}$$

The program (47) follows the standard mathematical program using the second-order cone programming, and details of its implementation can be found in [34].

5 Particle finite element method

The particle finite element method (PFEM) is a mixture of the particle approach and the Lagrangian FEM in the way that it treats mesh nodes as free particles [8] but solves the governing equations using the Lagrangian FEM. The essential step of the PFEM is the use of the alpha-shape method to identify the boundaries of computational domains followed by the mesh generation for the Lagrangian finite element analysis. More details on the PFEM can be found in [6,8,35,36]. The version of the PFEM developed in [6,17] is adopted in this paper. In a given time interval, the PFEM solution includes: (a) updating the mesh nodes location according to the incremental displacement obtained in the last analysis step; (b) identifying the boundary of the computational domain based on the updated mesh nodes by means of the alpha-shape technique; (c) Triangulation of the identified domain to generate new meshes; (d) Mapping the history field variables from the old mesh to the new mesh; and (e) Solving the equations over the new mesh using the Lagrangian FEM. Owing to step (b), the PFEM possesses the capability of modelling separation and reconnection of parts of the computational domain as well as single isolated particles [8] which may occur in fluid dynamics problems such as the breaking of a wave and water splashing and geotechnical problems such as dry granular flows and landslides. After the separation, the motion of an isolated particle is treated as freely falling body and can be solved analytically while the motion of a subdomain is solved via the FEM. When they are close to the major domain, the isolated particle and subdomain will be reconnected to the major domain when step (b) is operated. Note that the boundary detection using the alpha-shape method may cause volume variations (or the variation of the total mass) artificially. However, Numerical investigations indicate that the volume preservation can be kept within an acceptable range (below 2% for challenging fluid-structure problems) by using a proper value of alpha and mesh refinement [37].

It is notable that, although the developed formulation for dynamic analysis of saturated porous media is based on the small-deformation theory, the configuration of the material is updated after each incremental analysis. The idea of using a series of incremental analysis based on infinitesimal strain theory with an updated geometry for large deformation problems has been widely in the sequential limit analysis [38–40]. Later it has been adopted in the development of the so-called Remeshing and Interpolation Technique with Small Strain (RITSS) that has been applied successfully to various large deformation geotechnical problems [41–43]. Additionally, this idea has been adopted in the PFEM for modeling numerous challenging large deformation problems such as the breakage of a water dam, the granular column collapse, the underwater granular flow and induced waves [17] for which good agreements between the PFEM results and the lab testing data are obtained.

6 Numerical examples

In this section, the proposed finite element formulation and its PFEM version are used for the dynamic analysis of saturated porous media. A total of four examples are accounted for in this section. The 1D dynamic consolidation of a saturated soil column is simulated with emphases on the time integration scheme and simulation results are compared with analytical solutions and numerical results available in literature. Afterwards, wave propagations in a layer of saturated soils are considered where the validity of the developed mixed triangular elements overcoming pressure oscillation and the solution convergence with respect to mesh sizes are concerned. Displacement and pore water pressure are compared with available date in literature. A lab testing of the collapse of a saturated sand column in air is simulated as the third example to validate the proposed method for dynamic modelling of elastoplastic saturated porous media with large deformations. Simulation results are compared to both available data from lab tests and results from the material point method. The failure of an embankment is the fourth example where the PFEM simulation results are compared to the ones from the SPH modelling.

6.1 1D dynamic consolidation

The 1D dynamic consolidation problem is illustrated in Figure 3 where the saturated soil column is subjected to two loading types, namely $f_1(t)$ and $f_2(t)$.

Since the standard θ-method is employed for time discretization, the time integration scheme is implicit and unconditional stable if all three constants, θ_1, θ_2 and θ_3 (indicated by $\theta_{1,2,3}$ for brevity), are greater than or equal to 0.5 [44]. Otherwise, the time integration scheme is explicit. For $\theta_{1,2,3} = 0.5$, the integration scheme is the midpoint rule while it is the backward Euler scheme if $\theta_{1,2,3} = 1$. To illustrate the feature of the time integration scheme, the vertical loading $f_1(t)$ is applied at the surface of the soil column. Three sets of time integration parameters (e.g.

$\theta_{1,2,3} = 0.495, 0.5, 1.0$) are used. The time step is $\Delta t = 5 \times 10^{-3}$ s. The displacement at the top surface (e.g. point A (x = 1 m, y = 10 m)) and the pressure at the bottom (e.g. point B (x = 1 m, y = 0 m)) are monitored. The selected parameters are in line with these from [45]: density of the mixture $\rho = 2000\ \mathrm{kg/m^3}$, Young's modulus $E = 10^4$ kPa, Poisson's ratio $\upsilon = 0.2$, porosity $n_f = 0.35$, Darcy permeability is $k = 10^{-2}\ \mathrm{m/s}$.

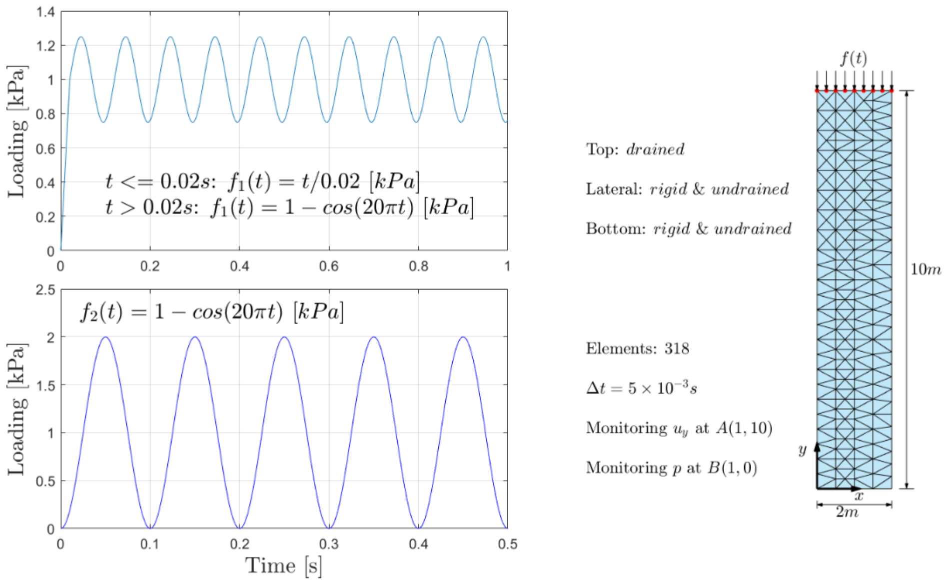

Figure 3. Set-up for 1D dynamic consolidation.

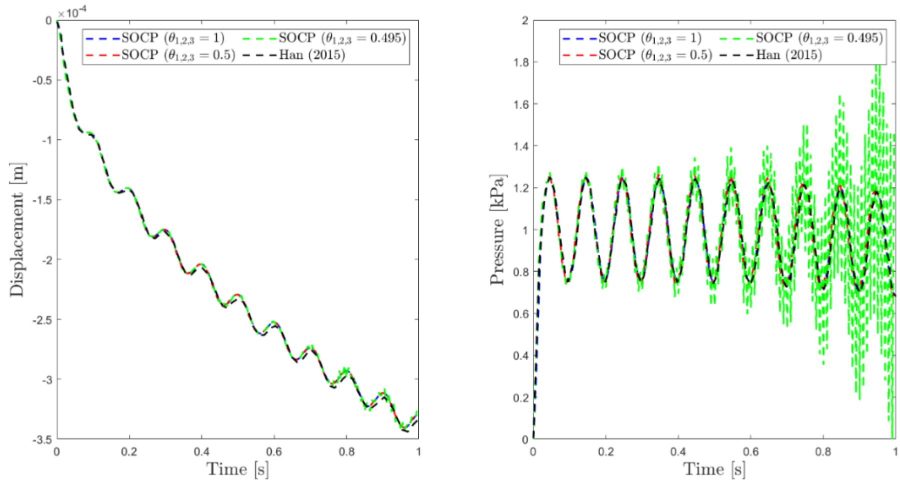

Figure 4. Time histories for displacement at Point A and pore water pressure at Point B for $k = 10^{-2}$ m/s in 1 second with $\Delta t = 0.005$ s.

As shown in Figure 4, stable solutions for both displacement and pore water pressure are ensured when using the value 0.5 and 1.0 for all time integration parameters (e.g. $\theta_{1,2,3} = 0.5$ and $\theta_{1,2,3} = 1.0$). For time integration parameters $\theta_{1,2,3} = 0.495$, the pore water pressure is severely oscillated from $t = 0.2$ s while unstable displacements are observed from $t = 0.75$ s. This phenomenon also agrees with the observation in [45] that the pressure response at point B is easier to be unstable compared to the displacement response at point A.

To investigate the convergence of the solution with respect to the time step, two other time steps (e.g. $\Delta t = 2.5 \times 10^{-3}$s and 1×10^{-2}s) are used to simulate the problem with time integration parameters $\theta_{1,2,3} = 0.5$ and 1.0, respectively. The simulation results are compared to the ones using $\Delta t = 5 \times 10^{-3}$s. As shown in Figure 5, satisfactory agreements are obtained for all cases. In the following, the time integration parameters $\theta_{1,2,3} = 1.0$ are selected for all simulations indicating the backward Euler scheme.

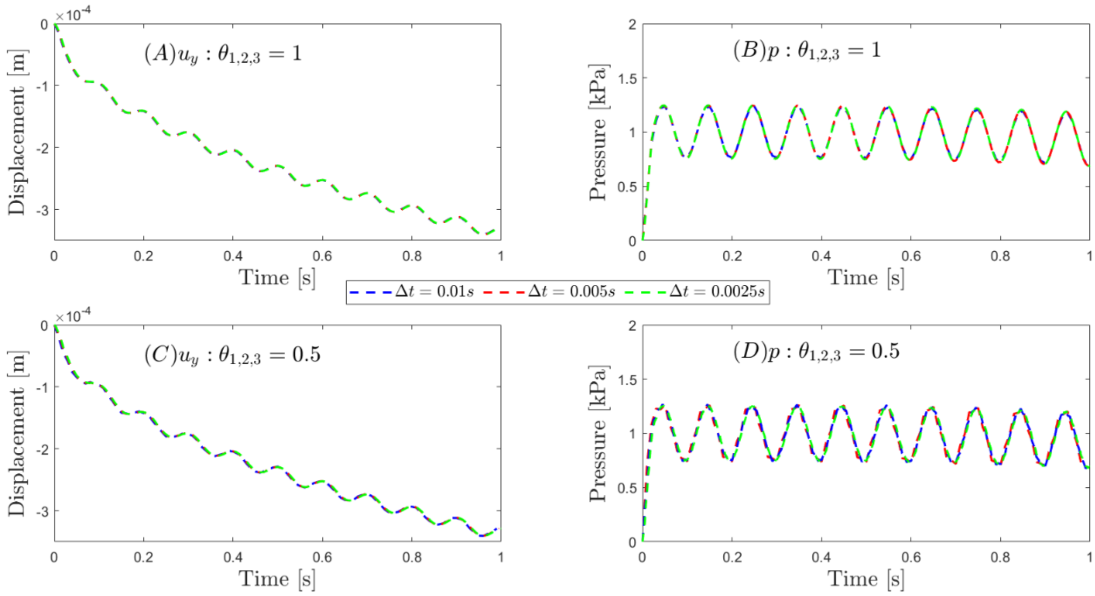

Figure 5. Evolution of displacement at Point A and pore water pressure at Point B from simulations using different time steps and time integration parameters.

The proposed formulation is further verified against the dynamic response of an infinite half-space subjected to surface loading for which the analytical solution is available [46,47]. The problem is treated as a plane-strain problem with the surface loading $f_2(t)$. The set-up of the problem is the same as that in [47] with the following material parameters: density of solid $\rho_s = 2000\ \mathrm{kg/m^3}$, density of fluid $\rho_f = 1000\ \mathrm{kg/m^3}$, porosity $n_f = 0.33$, Lamé constants of solid skeleton $\mu^s = 5.583\ \mathrm{MPa}$ and $\lambda^s = 8.375\ \mathrm{MPa}$. The dynamic response in terms of the displacement at the top surface obtained from the proposed formulation is compared with the analytical solution from [47] where a great agreement is obtained.

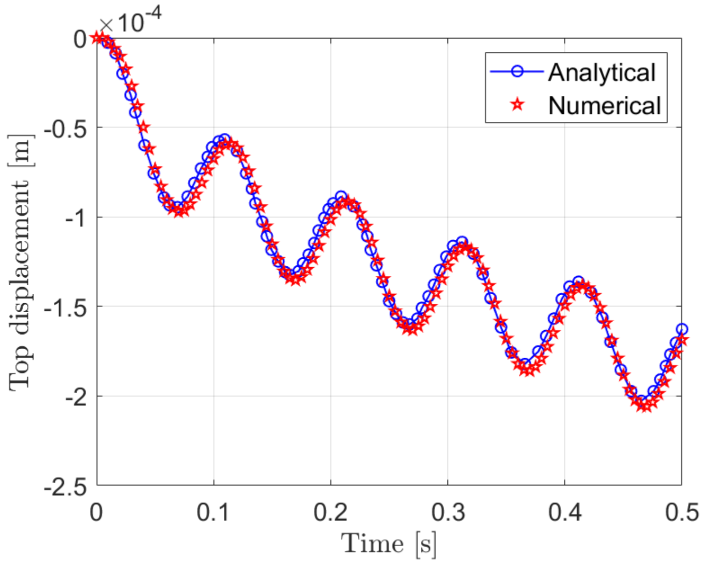

Figure 6. Top displacement history at Point A for $k = 10^{-2}$ m/s in 0.5 seconds. The analytical result is from [47].

6.2 2D wave propagation

In this example, the wave propagation in a rectangular saturated poroelastic medium (21 m long and 10 m deep) studied in [47] is concerned. The illustration of the problem is shown in Figure 7. The medium is subjected to a surface loading with a width W_f = 1 m. Material parameters are the same as the ones used in the analytical example in section 6.1 which are also in line with these in [47]. The input force, lasting for 0.04 s, is

$$f(t) = 10^2 \sin(25\pi t)\, H(t - 0.04) \quad [kPa] \tag{50}$$

in which H denotes the Heaviside step function (see also Figure 7).

Evolution of the displacement at Point A and pressure at Point B are monitored (see also

Figure 7). Three mesh configurations with the length of mesh edge h_e being $1/2W_f$ (MESH1), $1/4W_f$ (MESH2), and $1/8W_f$ (MESH3) are used for investigating solution convergence with respect to mesh size. A fixed time step of 5×10^{-4} s is adopted in all simulations.

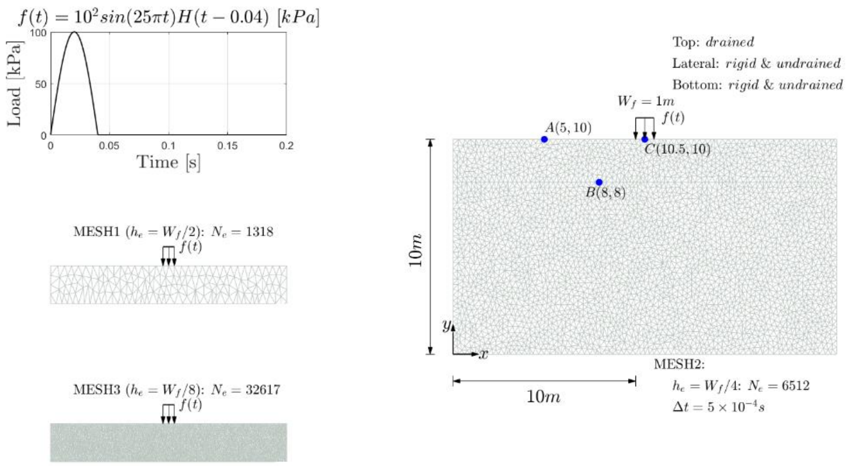

Figure 7. Illustration of 2D wave propagation in a rectangular domain with three mesh configurations MESH1, MESH2 and MESH3. The loading function is shown in the left-top sub-figure, and the mesh density of MESH1 and MESH3 in a section (y ≥ 8 m) of the domain is also presented.

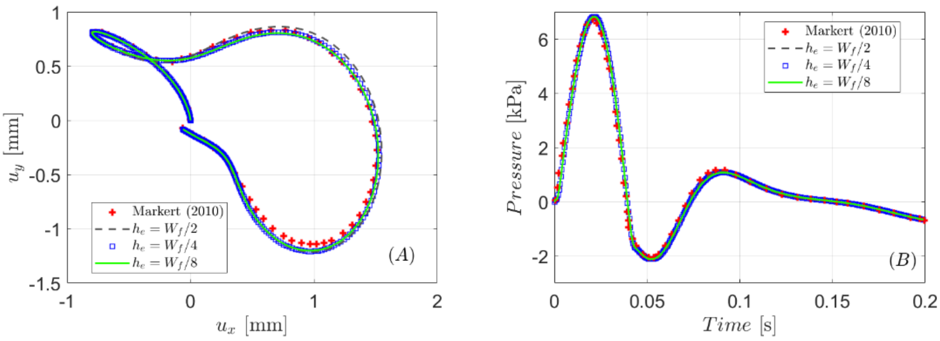

Figure 8. The motion of Point A and the pore water pressure evolution at Point B.

The curves displayed in Figure 8 (A) depict the in-plane motion of Point A from 0 to 0.2 s. The trajectories of Point A obtained using different meshes agree with each other which are also consistent with the published results in [47,48]. Figure 8 (B) shows the evolution of the pore water pressure at Point B, and the good agreement also verifies our formulation.

The wavefields of the total displacement at different scenarios are illustrated in Figure 9 which are similar to these found in [47–49]. The pressure field at t = 0.05 s is illustrated in Figure 10 in which the simulation results from [48] are also illustrated. Note that an additional stabilization technique is required to ensure the stability of pore water pressure in [48] since linear elements are used. In contrast, the stabilization technique is not necessitated for the proposed formulation because quadratic interpolations are used for displacement-like fields and linear interpolations are for stress-like fields in the element (see also Figure 2).

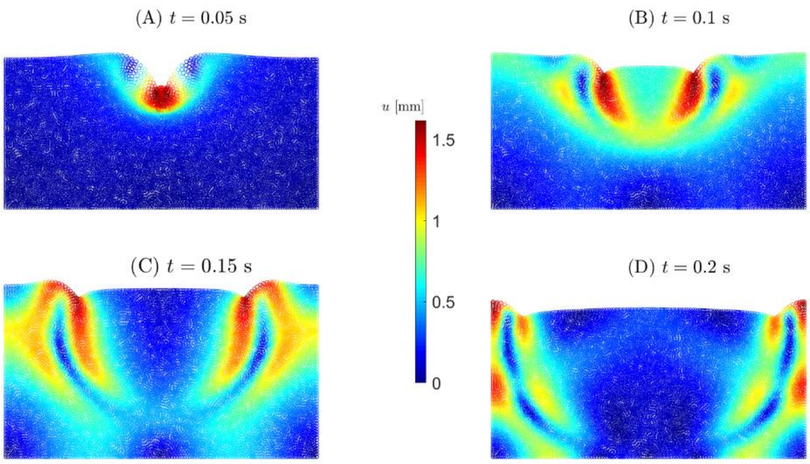

Figure 9. Wavefields of the total displacement at four instants from the simulation with

MESH2 ($h_e = W_f/4$). The deformed mesh is rescaled with a factor of 500.

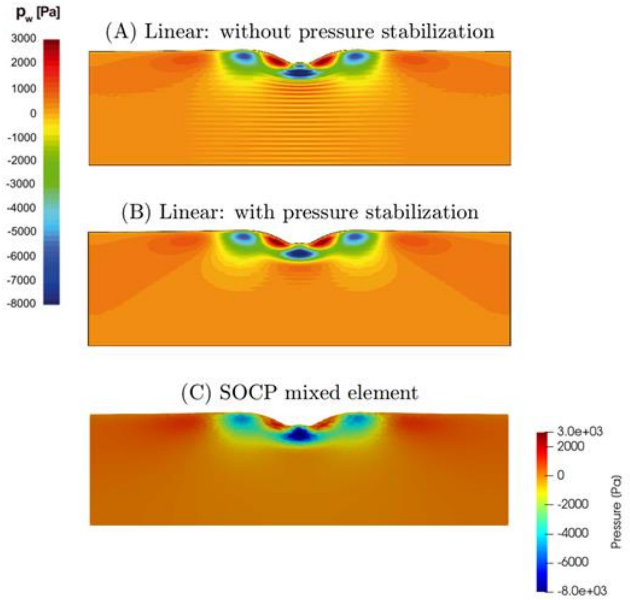

Figure 10. Wavefields of pore water pressure at t = 0.05 s: (A) without stabilization technique from [48]; (B) with pressure stabilization technique from [48]; (C) from the proposed formulation with the mixed triangular element. Deformation is scaled by a factor of 250.

6.3 Collapse of a saturated granular column in air

The experiment of the granular column collapse has been widely used to investigate the mechanism of many geophysical phenomena due to its similarity to rapid movements of mass flows, such as landslides, debris flows and avalanches. In this part, the proposed numerical method is applied to a recent experimental study of the collapse of a saturated granular column in air [50]. Here we reproduce this experiment with one configuration in [50] to verify the correctness of the proposed method. The experiment set-up is illustrated in Figure 11 in which the saturated column collapses in a flume after removing the gate.

Figure 11. Illustration of the experiment set-up in [50] used for saturated column collapse tests. The case selected has a geometry of $L_0 = 4$ cm and $H_0 = 6$ cm.

In the simulation, the saturated granular column is discretized into two configurations: (i) 4000 elements (dense mesh) and (ii) 2507 elements (coarse mesh). The adopted material parameters are from [50]: density of solid $\rho_s = 2600\ \mathrm{kg/m^3}$, density of fluid $\rho_f = 1000\ \mathrm{kg/m^3}$, porosity $n_f = 0.4$, Poisson's ratio $\upsilon = 0.3$, elastic modulus $E = 10\ \mathrm{MPa}$, effective cohesion $c' = 0$ Pa and effective friction angle $\varphi' = 35^\circ$. The dilation angle is set as $\psi = 0^\circ$. The Darcy permeability is computed through the Kozeny-Carman equation [50]:

$$k = \frac{k_L g}{\eta_d} \text{ with } k_L = \frac{D^2}{150} n_f^3 / (1 - n_f)^2 \tag{51}$$

where D is the mean diameter of the granular material, k_L is the intrinsic permeability and η_d is the dynamic viscosity for fluid. The measured value of D is 2.5 mm. The dynamic viscosity η_d for water is chosen as a typical value of 10^{-3} Pa · s. The bottom of the column is fully fixed while the left side is fixed in horizontal direction. The gravity loading is first applied to generate stresses with the gate being fixed. In this gravitational step, only the top surface of the column is set as drainable. After that, the gate is removed to release the granular column. Meanwhile, the surfaces exposed to air are set as drainable. To save computational cost, an adaptive time step is used in the way that the maximum incremental displacement at each step is smaller than the length of the mesh edge.

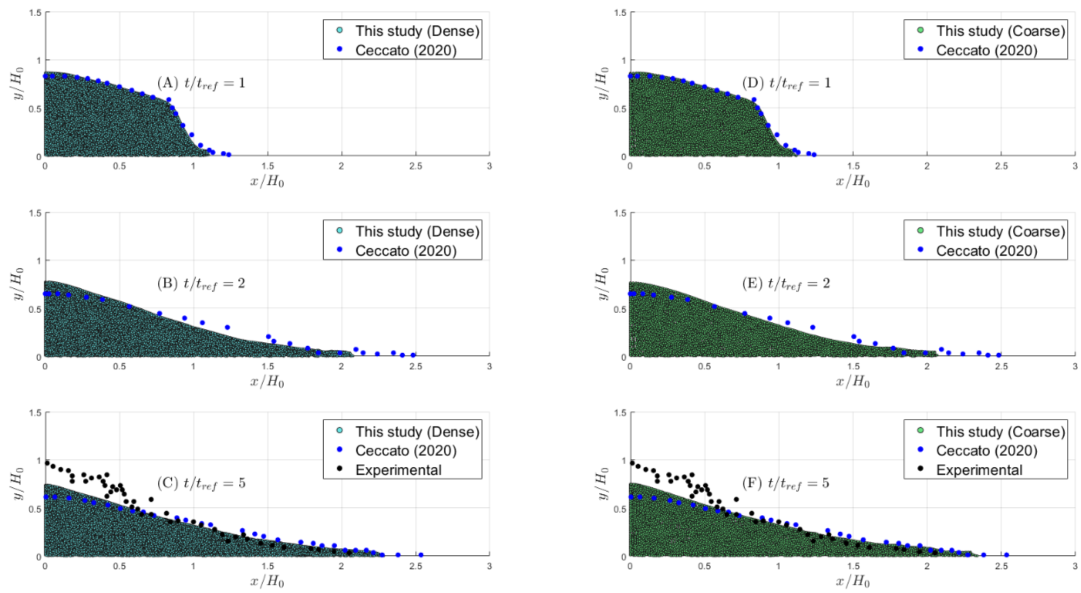

Figure 12. Simulation results from this study using coarse and dense meshes compared with MPM and experimental results from [50] at three instants.

Figure 12 shows the scenarios of the collapse at three instants $\frac{t}{t_{ref}} = 1, 2, 5$, respectively, where the reference time is $t_{ref} = \sqrt{H_0/g'}$ and the reduced gravity acceleration is computed by $g' = g(\rho_s - \rho_f)/\rho_s$. It can be seen that the simulation results obtained from two mesh configurations in this study agree well with the MPM results in [50], which verifies the proposed version of the PFEM for dynamic analysis of saturated porous media with large deformations. However, a visible difference exists between the simulated final deposit and experimental data which may be attributed to the complex behavior of saturated medium during rapid movement in reality and further studies are required to provide a more reasonable constitutive relationship.

6.4 Embankment failure

The failure of an embankment is studied using the proposed PFEM in this section with simulation results compared to these from the classical Bishop's method and the SPH method. The concerned embankment is a two-sided model and triggered by the difference of pore water pressure between the high reservoir water level on the left hand side and the low ground water table on the right hand side. The model of the embankment is from [51] and illustrated in Figure 13. Instead of prescribing pore water pressure boundary condition along the embankment surface in [51], the water region is part of our simulation. Nevertheless, the direct enforcement of the pore water pressure on the embankment is also possible in the proposed approach.

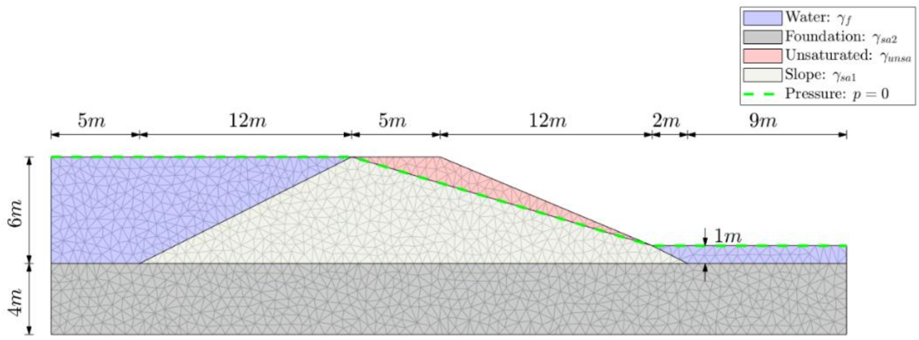

Figure 13. Two-sided slope embankment model from [51]. The model is discretized using 2277 elements. Lateral boundaries are set as free-roller and the bottom is fixed in the simulation.

As shown in Figure 13, the model consists of four parts: water, foundation (saturated), unsaturated soil and slope (saturated), marked in different colors. The unsaturated soil is treated as dry for the sake of simplicity which is in line with the assumption made in [51]. The groundwater table is represented as a green dashed line in Figure 13. The parameters are as given in [51]: unit weight of the water $\gamma_f = 10\ \mathrm{kN/m^3}$, unit weight of the unsaturated soil $\gamma_{unsa} = 18.5\ \mathrm{kN/m^3}$, unit weight of the saturated soil in the slope $\gamma_{sa1} = 20\ \mathrm{kN/m^3}$, unit weight of the saturated soil in the foundation $\gamma_{sa2} = 22\ \mathrm{kN/m^3}$. For the saturated and unsaturated soils in the slope, elastic modulus is $E_1 = 25$ MPa, internal friction angle is $\varphi_1 = 22^{\circ}$, cohesion is $c_1 = 4$ kPa, dilation angle is $\psi_1 = 0^{\circ}$ and Poisson's ratio is $\upsilon_1 = 0.3$. For foundation soils, we have $E_2 = 50$ MPa, $\varphi_2 = 22^{\circ}$, $c_2 = 10$ kPa, $\psi_2 = 0^{\circ}$ and $\upsilon_2 = 0.3$. As for water, both the cohesion and friction angle are set as zero as in [17], and the Poisson's ratio is set as 0.499 to approximate the non-compressibility.

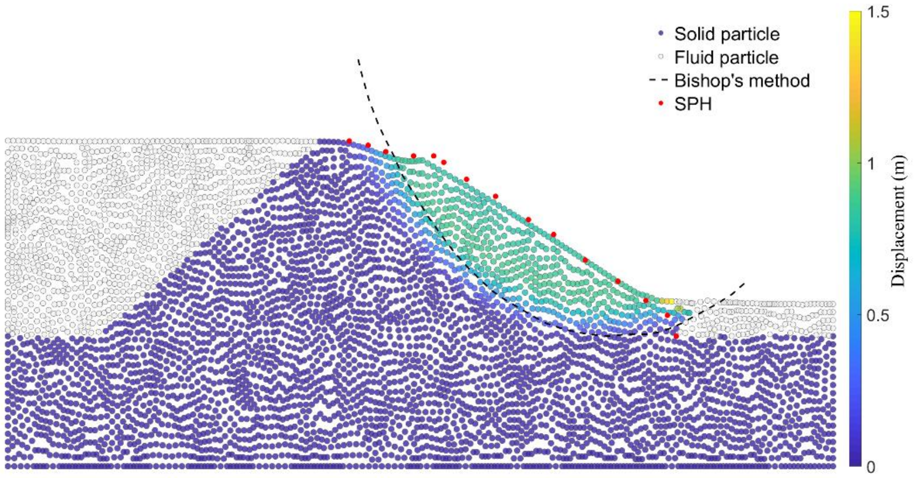

Figure 14. Final deposit profile with displacement distribution after the slope failure. The data of Bishop's method and SPH result are extracted from [51].

The whole model is set as stable during the gravitation loading step by adopting a large cohesion and an internal friction angle. Then dynamic analysis is performed by decreasing the strength to the specified value which triggers the failure of the embankment. The dynamic analysis is carried out using a time step Δt = 0.01 s. The final deposit profile obtained from our simulation agrees well with that from the SPH modelling and the shear band also agrees with the classical Bishop's slip surface from [51], indicating the correctness of the proposed method for dynamic analysis of embankment consisting of saturated soils.

7 Conclusions

In this paper, a generalized Hellinger-Reissner (HR) variational principle is developed for dynamic analysis of saturated porous media. With a proposed mixed finite element, the variational principle leads to a min-max optimization problem which can be reformed as a standard second-order cone programming problem to be resolved efficiently using an advanced optimization algorithm. To enable the large deformation analysis, the formulation is further merged into the PFEM framework. The correctness of the proposed formulation has been validated against the benchmark of the dynamic consolidation and the wave propagation in saturated soils. It is shown that the simulation results agree well with the analytical solution and with these from conventional finite element analysis. The capability of the proposed PFEM version for large deformation dynamic analysis of saturated porous media is also illustrated by simulating the collapse of a saturated granular column in air and the post-failure of an embankment owing to seepage with results being compared to these from lab testing and the numerical modelling using the material point method and the smoothed particle hydrodynamics method.

Acknowledgements

The author Liang Wang greatly appreciates the financial support from the cooperation agreement between the University of Bologna and the China Scholarship Council (No. 201606060161).

References

[1] Nazem M, Sheng D, Carter JP, Sloan SW. Arbitrary Lagrangian–Eulerian method for large-strain

consolidation problems Majidreza. Int J Numer Anal Methods Geomech 2008;32:1023–50.

[2] Peng C, Wu W, Yu H sui, Wang C. A SPH approach for large deformation analysis with hypoplastic constitutive model. Acta Geotech 2015;10:703–17.

[3] Bui HH, Fukagawa R, Sako K, Wells JC. Slope stability analysis and discontinuous slope failure simulation by elasto-plastic smoothed particle hydrodynamics (SPH). Géotechnique 2011;61:565–74.

[4] Soga K, Alonso E, Yerro A, Kumar K, Bandara S, Kwan JSH, et al. Trends in large-deformation analysis of landslide mass movements with particular emphasis on the material point method. Géotechnique 2016;66:248–73.

[5] Tran QA, Sołowski W. Generalized Interpolation Material Point Method modelling of large deformation problems including strain-rate effects – Application to penetration and progressive failure problems. Comput Geotech 2019;106:249–65.

[6] Zhang X, Krabbenhoft K, Pedroso DM, Lyamin A V., Sheng D, Vicente da Silva M, et al. Particle finite element analysis of large deformation and granular flow problems. Comput Geotech 2013;54:133–42.

[7] Oñate E, Celigueta MA, Idelsohn SR, Salazar F, Suárez B. Possibilities of the particle finite element method for fluid-soil-structure interaction problems. Comput Mech 2011;48:307–18.

[8] Oñate E, Idelsohn SR, Del Pin F, Aubry R. The particle finite element method-an Overview. Int J Comput Methods 2004;1:267–307.

[9] Idelsohn SR, Oñate E, Del Pin F. The particle finite element method: A powerful tool to solve incompressible flows with free-surfaces and breaking waves. Int J Numer Methods Eng

2004;61:964–89.

[10] Carbonell JM, Oñate E, Suárez B. Modeling of ground excavation with the particle finite-element method. J Eng Mech 2010;136:455–63.

[11] Cante J, Dávalos C, Hernández JA, Oliver J, Jonsén P, Gustafsson G, et al. PFEM-based modeling of industrial granular flows. Comput Part Mech 2014;1:47–70.

[12] Dávalos C, Cante J, Hernández JA, Oliver J. On the numerical modeling of granular material flows via the Particle Finite Element Method (PFEM). Int J Solids Struct 2015;71:99–125.

[13] Zhang X, Krabbenhoft K, Sheng D. Particle finite element analysis of the granular column collapse problem. Granul Matter 2014;16:609–19.

[14] Salazar F, Irazábal J, Larese A, Oñate E. Numerical modelling of landslide-generated waves with the particle finite element method (PFEM) and a non-Newtonian flow model. Int J Numer Anal Methods Geomech 2015;40:809–26.

[15] Cremonesi M, Ferri F, Perego U. A basal slip model for Lagrangian finite element simulations of 3D landslides. Int J Numer Anal Methods Geomech 2017;41:30–53.

[16] Zhang X, Krabbenhoft K, Sheng D, Li W. Numerical simulation of a flow-like landslide using the particle finite element method. Comput Mech 2015;55:167–77.

[17] Zhang X, Oñate E, Torres SAG, Bleyer J, Krabbenhoft K. A unified Lagrangian formulation for solid and fluid dynamics and its possibility for modelling submarine landslides and their consequences. Comput Methods Appl Mech Eng 2019;343:314–38.

[18] Franci A, Zhang X. 3D numerical simulation of free-surface Bingham fluids interacting with

structures using the PFEM. J Nonnewton Fluid Mech 2018;259:1–15.

[19] Monforte L, Arroyo M, Carbonell JM, Gens A. Numerical simulation of undrained insertion problems in geotechnical engineering with the Particle Finite Element Method (PFEM). Comput Geotech 2017;82:144–56.

[20] Monforte L, Arroyo M, Carbonell JM, Gens A. Coupled effective stress analysis of insertion problems in geotechnics with the Particle Finite Element Method. Comput Geotech 2018;101:114–29.

[21] Yuan WH, Zhang W, Dai B, Wang Y. Application of the particle finite element method for large deformation consolidation analysis. Eng Comput (Swansea, Wales) 2019;36:3138–63.

[22] Tits AL, Wachter A, Bakhtiari S, Urban TJ, Lawrence CT. A primal-dual intertior-point method for nonlinear programming with strong global and local convergence properties. SIAM J Optim 2003;14:173–99.

[23] Alizadeh F, A. Haeberly J-P, L. Overton M. Primal-dual interior-point methods for semidefinite programming: convergence rates, stability and numerical results. SIAM J Optim 1998;8:746–68.

[24] Krabbenhøft K, Lyamin A V., Sloan SW. Formulation and solution of some plasticity problems as conic programs. Int J Solids Struct 2007;44:1533–49.

[25] Washizu K. Variational Methods in Elasticity and Plasticity. 3rd ed. New York: Pergamon Press; 1982.

[26] Zhang X, Sheng D, Sloan SW, Bleyer J. Lagrangian modelling of large deformation induced by progressive failure of sensitive clays with elastoviscoplasticity. Int J Numer Methods Eng 2017;112:963–89.

[27] Zhang X, Sheng D, Sloan SW, Krabbenhoft K. Second-order cone programming formulation for consolidation analysis of saturated porous media. Comput Mech 2016;58:29–43.

[28] Reissner E. On a variational theorem in elasticity. J Math Phys 1950;29:90–5.

[29] Zienkiewicz O, Chan A, Pastor M, Schrefler B, Shiomi T. Computational geomechanics with special reference to earthquake engineering. New York: John Wiley & Sons; 1999.

[30] Chen J, Dargush GF. Boundary element method for dynamic poroelastic and thermoelastic analyses. Int J Solids Struct 1995;32:2257–78.

[31] Boyd S, Vandenberghe L. Convex optimization. New York: Cambridge University Press; 2004.

[32] Krabbenhoft K, Karim MR, Lyamin A V, Sloan SW. Associated computational plasticity schemes for nonassociated frictional materials. Int J Numer Methods Eng 2012;90:1089–117.

[33] Wang D, Chen X, Yu Y, Jie Y, Lyu Y. Stability and Deformation Analysis for Geotechnical Problems with Nonassociated Plasticity Based on Second-Order Cone Programming. Int J Geomech 2018;19:1–13.

[34] Wang L, Zhang X, Zaniboni F, Oñate E, Tinti S. Mathematical optimization problems for particle finite element analysis applied to 2D landslide modeling. Math Geosci 2019:1–23.

[35] Cremonesi M, Frangi A, Perego U. A Lagrangian finite element approach for the analysis of fluid–structure interaction problems. Int J Numer Methods Eng 2010;84:610–30.

[36] Zhang W, Yuan W, Dai B. Smoothed particle finite-element method for large-deformation problems in geomechanics. Int J Geomech 2018;18.

[37] Franci A, Cremonesi M. On the effect of standard PFEM remeshing on volume conservation in

free-surface fluid flow problems. Comput Part Mech 2017;4:331–43.

[38] Yang WH. Large deformation of structures by sequential limit analysis. Int J Solids Struct 1993;30:1001–13.

[39] Leu SY. Convergence analysis and validation of sequential limit analysis of plane-strain problems of the von Mises model with non-linear isotropic hardening. Int J Numer Methods Eng 2005;64:322–34.

[40] Kong D, Martin CM, Byrne BW. Sequential limit analysis of pipe-soil interaction during large-amplitude cyclic lateral displacements. Géotechnique 2018;68:64–75.

[41] Hu Y, Randolph MF. A practical numerical approach for large deformation problems in soil. Int J Numer Anal Methods Geomech 1998;22:327–50.

[42] Tian Y, Cassidy MJ, Randolph MF, Wang D, Gaudin C. A simple implementation of RITSS and its application in large deformation analysis. Comput Geotech 2014;56:160–7.

[43] Wang D, Hu Y, Randolph MF. Three-dimensional large deformation finite-element analysis of plate anchors in uniform clay. J Geotech Geoenvironmental Eng 2010;136:355–65.

[44] Gear CW. Numerical initial value problems in ordinary differential equations. New Jersey: Prentice Hall PTR; 1971.

[45] Han B, Zdravkovic L, Kontoe S. Stability investigation of the Generalised-α time integration method for dynamic coupled consolidation analysis. Comput Geotech 2015;64:83–95.

[46] Essen R de B, Ehlers W, Liu Z. One-dimensional transient wave propagation in fluid-saturated incompressible porous media. Arch Appl Mech 1993;63:59–72.

[47] Markert B, Heider Y, Ehlers W. Comparison of monolithic and splitting solution schemes for dynamic porous media problems. Int J Numer Methods Eng 2010:1341–83.

[48] Monforte L, Navas P, Carbonell JM, Arroyo M, Gens A. Low-order stabilized finite element for the full Biot formulation in soil mechanics at finite strain. Int J Numer Anal Methods Geomech 2019;43:1488–515.

[49] Turek S, Obaid A, Markert B. On a fully implicit, monolithic finite element method-multigrid solution approach for dynamic porous media problems. J Coupled Syst Multiscale Dyn 2013;1:224–40.

[50] Ceccato F, Leonardi A, Girardi V, Simonini P, Pirulli M. Numerical and experimental investigation of saturated granular column collapse in air. Soils Found 2020;60:683–96.

[51] Bui HH, Fukagawa R. An improved SPH method for saturated soils and its application to investigate the mechanisms of embankment failure: case of hydrostatic pore-water pressure. Int J Numer Anal Methods Geomech 2013;37:31–50.